

Nodal higher-order topological superconductivity from C_6 -symmetric Dirac semimetals

Guan-Hao Feng¹

¹*School of Physical Science and Technology, Lingnan Normal University, Zhanjiang, 524048, China**
(Dated: August 22, 2024)

Three-dimensional Dirac semimetals (DSMs) have been shown to exhibit one-dimensional hinge modes which are termed the higher-order hinge Fermi-arc (HOFA) states. They are the topological consequences of Dirac points. Superconducting states from Dirac semimetals can inherit the Dirac points to form nodal Dirac superconducting states, raising a question of whether there exists a topological superconducting bulk-hinge correspondence similar to DSMs. In this work, we discuss the nodal superconducting states from half-filled DSMs respecting non-magnetic (Type-II) Shubnikov space group (SSG) $P6/mmm1'$. We find that the BdG Dirac points can lead to higher-order topological Dirac superconducting (HOTDSC) states instead of the expected higher-order Majorana-arc (HOMA) states. The HOTDSC states can be regarded as a crossing between the HOFAs in normal states and the BdG shadow states. We demonstrate that HOTDSC states can be indicated by relative topologies of BdG Dirac points by utilizing the theory of magnetic topological quantum chemistry (MTQC).

I. INTRODUCTION

Topological semimetals are bulk-gapless materials with topological boundary modes [1]. After the discovery of the 2D DSM graphene which exhibits 1D arc-like boundary states along zigzag edges [2], 3D nodal semimetals have attracted much attention due to their novel topological surface states [3–6]. For example, Weyl semimetals host Fermi-arc surface states [7], and centrosymmetry nodal-line semimetals host drumhead surface states [8]. From the perspective of the theory of electronic band structure (BS), despite the presence of nodal points in these semimetals, bands are still gapped away from nodal points in the Brillouin zone (BZ), such that the topological invariants are well-defined to allow for the existence of topological surface states. However, in the presence of the time-reversal and inversion symmetries, the Fermi-arc surface states in 3D DSMs are not topologically protected since the Dirac cones are not the source of Berry curvature. Despite the absence of topological surface states, it has been recently shown that for certain DSMs, intrinsic polarization-nontrivial HOFA states are the direct topological consequences of the Dirac cones [9–11]. Regarding one of the momenta as cyclic tuning parameters, the 2D subsystems can be viewed as topological (crystalline) insulators when the tunable momentum is away from the Dirac points [12]. Such that the Dirac points are the critical points between two different topological (crystalline) insulating states. When the 2D subsystems are either obstructed atomic limit or fragile topological states with intrinsic 0D corner modes [13–17], the nontrivial pumping cycles of these 2nd-order topological states are equivalent to 3D DSMs with HOFA states [9]. Thus the HOFA states can be indicated by the 2D filling anomaly of the subsystems, which can be calculated by the theory of MTQC [18–23].

These Dirac cones can be inherited by the superconducting states which may lead to HOMA states [24–26]. The superconductors with BdG Dirac points are termed the nodal Dirac superconductors [27, 28]. Similar to HOFA states, HOMA states are related to the 0D Majorana corner modes [29] and can be indicated by 2D BdG filling anomalies. However, not all the nodal Dirac superconductors exhibit HOMAs. For example, the nodal Dirac superconducting states respecting Type-II SSG $P4/mmm1'$ can host HOMA states in odd-parity pairing channels [26], whereas the nodal Dirac superconducting states respecting $P6/mmm1'$ can only host HOTDSC states at the time-reversal invariant planes [24]. The different topological properties of the BdG Dirac points have thus remained an open question as to how the BdG Dirac points can exhibit higher-order topology inherited from the Dirac points in normal states.

In Ref. [11], the relative topology is employed to classify the Dirac points in normal states with or without HOFA states. The relative topology concerns if two states separated by a bulk nodal point are topologically distinct when all the symmetries are preserved throughout the deforming process [30], which can be indicated by changes in topological invariants. In this work, we advance the relative topology to BdG Dirac points and employ the theory of MTQC to discuss the possible higher-order topological states in nodal Dirac superconductors respecting Type-II SSG $P6/mmm1'$. Given that the conventional (double) symmetry indicators (SIs) [31–33] used in insulators fall short in distinguishing various topological superconductors such as the 1D Kitaev chain [34–36], we introduce the refined SIs in Ref. [37]. By calculating the difference of refined SIs and BdG filling anomalies between two sides of a BdG Dirac point, we can determine the occurrence of HOMA or HOTDSC states. We note that although higher-order topological phases can occur in both crystalline and non-crystalline systems [38–41], the relative topology here is only applicable to

* fenggh@lingnan.edu.cn

crystalline systems.

Our results show that the BdG Dirac points can be grouped into two types: symmetry-enforced BdG Dirac points and non-symmetry-enforced (accidental) BdG Dirac points. A symmetry-enforced BdG Dirac point arises from the crossing of two distinct band corepresentations (coreps) and the relative topology is nontrivial, whereas the non-symmetry-enforced BdG Dirac point arises from the crossing of two identical band representations and the relative topology is trivial. We find that 3D nodal Dirac superconductors respecting Type-II SSG $P6/mmm1'$ cannot host HOMA states since that all the refined SIs of the 2D planes with $k_z \neq 0, \pi$ vanish. Instead, for symmetry-enforced nodal Dirac superconducting states, there are HOTDSC states at the time-reversal invariant planes only if the corresponding normal state is HOFA state and the pairing channels are B_{1u} or B_{2u} . Interestingly, we demonstrate that the HOFA states in normal states are obstructed atomic limit states whereas the HOTDSC states are fragile topological states. The HOTDSC states arise from the crossing between the HOFAs in the normal states and those in the corresponding BdG shadow states. Thus the HOTDSC states can be viewed as a manifestation of a bulk-hinge correspondence for the 3D nodal Dirac superconductors respecting Type-II SSG $P6/mmm1'$.

This paper is organized as follows. In Sec. II, we briefly review the concept of compatibility relations used to determine the occurrence of Dirac points in normal states. To identify the HOFA DSMs, we utilize the theory of MTQC to calculate the symmetry indicators and filling anomalies of the 2D slices with fixed k_z and discuss the relative topologies of the Dirac points. In Sec. III, we extend the application of compatibility relations to BdG systems. We analyze the origin of the BdG Dirac points by using the compatibility relations. We then classified the BdG Dirac points by whether they arise from different band coreps or not. We calculate the relative topologies of the symmetry-enforced BdG Dirac points in each pairing channel and summarize the possible HOTDSC states in Supplementary Note 8. This is the main result of this work. In Sec. IV, we construct a 3D DSM tight-binding model and introduce the possible superconducting pairing channels. We discuss the possible higher-order topological phases by numerical calculations. The results are consistent with our conclusions in Sec. III.

II. COMPATIBILITY RELATIONS AND HOFA DSMS

In this section, we will briefly review the concept of compatibility relations which are used to determine the occurrence of symmetry-enforced Dirac points in momentum space. For Type-II double SSG $P6/mmm1'$, at a given momentum point \mathbf{k} in the first BZ, as shown in Fig. 1, the Bloch eigenstates can be labeled by the

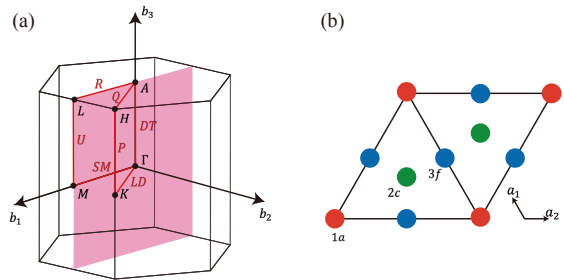


FIG. 1. (a) The BZ of space group $P6/mmm$. In this paper, we label the high-symmetry points and lines in reduced coordinates with $b_1 = (0, 4\pi/\sqrt{3}, 0)$, $b_2 = (2\pi, 2\pi/\sqrt{3}, 0)$, and $b_3 = (0, 0, 2\pi)$. The red area is the BZ of the subsystem in ribbon geometry when we terminate the 3D lattice in the a_2 direction. (b) The maximal Wyckoff positions of space group $P6/mmm$ in the 2D plane with $z = 0$. The lattice vectors are given by $a_1 = (-1/2, \sqrt{3}/2, 0)$, $a_2 = (1, 0, 0)$, and $a_3 = (0, 0, 1)$. Here we have set all the lattice constants to 1. All the notations are given in the convention of BCS [42, 43].

small coreps $u_{\mathbf{k}}^{\alpha}$ of the little group $G_{\mathbf{k}}$. The superscript α labels the distinct irreducible coreps. We first list the arms of the high-symmetry line momentum stars, i.e., $\mathbf{k}_{DT} = (0, 0, w)$, $\mathbf{k}_P = (1/3, 1/3, w)$, $\mathbf{k}_{LD} = (u, u, 0)$, $\mathbf{k}_Q = (u, u, 1/2)$, $\mathbf{k}_R = (u, 0, 1/2)$, $\mathbf{k}_{SM} = (u, 0, 0)$, and $\mathbf{k}_U = (1/2, 0, w)$ in reduced coordinates. The occurrence of Dirac points at these high-symmetry lines are determined by BS and the compatibility relations of these arms.

Specifically, to determine whether there are Dirac points present along the high-symmetry line DT, we can use the small corep compatibility relations between the high-symmetry points $\mathbf{k}_{\Gamma} = (0, 0, 0)$ and $\mathbf{k}_A = (0, 0, 1/2)$, which are tabulated on the Bilbao Crystallographic Server (BCS) [42, 43]:

$$\begin{aligned}
 \bar{\Gamma}_7 \downarrow G_{DT} &= \bar{A}_7 \downarrow G_{DT} = \overline{DT}_7, \\
 \bar{\Gamma}_8 \downarrow G_{DT} &= \bar{A}_8 \downarrow G_{DT} = \overline{DT}_8, \\
 \bar{\Gamma}_9 \downarrow G_{DT} &= \bar{A}_9 \downarrow G_{DT} = \overline{DT}_9, \\
 \bar{\Gamma}_{10} \downarrow G_{DT} &= \bar{A}_{10} \downarrow G_{DT} = \overline{DT}_7, \\
 \bar{\Gamma}_{11} \downarrow G_{DT} &= \bar{A}_{11} \downarrow G_{DT} = \overline{DT}_8, \\
 \bar{\Gamma}_{12} \downarrow G_{DT} &= \bar{A}_{12} \downarrow G_{DT} = \overline{DT}_9.
 \end{aligned} \tag{1}$$

When two different small coreps cross in BS, the symmetry-enforced Dirac points would occur. For example, as shown in Fig. 2, when the subduced small coreps of the valence bands at DT with $k_z = k_0 - \delta k_z$ are \overline{DT}_9 and with $k_z = k_0 + \delta k_z$ are \overline{DT}_7 , there must be a symmetry-enforced Dirac point occurring at $k_z = k_0$. By regarding k_z as a cyclic tuning parameter, the presence of symmetry-enforced Dirac points can be indicated by the change in subduced small coreps of valence bands ($\overline{DT}_9 \rightarrow \overline{DT}_7$) in 2D geometry as

$$\bar{\Gamma}_9 \rightarrow \bar{\Gamma}_7 \tag{2}$$

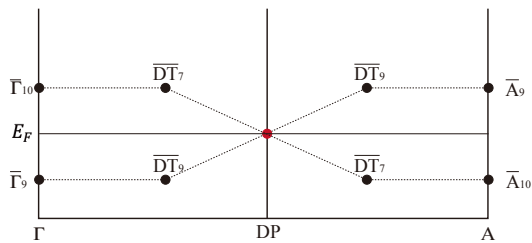


FIG. 2. Compatibility relations of the co-representations of a half-filling DSM system respecting Type-II SSG $P6/mmm1'$. There is a symmetry-enforced Dirac point (red dot) along DT which arises from the crossing of the irreps $\bar{D}\bar{T}_7$ and $\bar{D}\bar{T}_9$. We assume that the symmetry-enforced Dirac point (DP) locates at $\mathbf{k}_0 = (0, 0, k_0)$.

when we turn $k_z = k_0 - \delta k_z$ to $k_0 + \delta k_z$.

Similar discussion also applies to the high-symmetry line P, whose small corep compatibility relations between the high-symmetry point $\mathbf{k}_K = (1/3, 1/3, 0)$ and $\mathbf{k}_H = (1/3, 1/3, 1/2)$ are given by

$$\begin{aligned} \bar{K}_7 \downarrow G_P &= \bar{H}_7 \downarrow G_P = \bar{P}_4 \bar{P}_5, \\ \bar{K}_8 \downarrow G_P &= \bar{H}_8 \downarrow G_P = \bar{P}_6, \\ \bar{K}_9 \downarrow G_P &= \bar{H}_9 \downarrow G_P = \bar{P}_6. \end{aligned} \quad (3)$$

Thus the Dirac points can also occur along the high-symmetry line P when the two small coreps \bar{P}_6 and $\bar{P}_4 \bar{P}_5$ cross.

However, for the high-symmetry lines LD, Q, R, SM, and U, there is only one small corep for each high-symmetry line, which means that the compatibility relations are always satisfied and no symmetry-enforced Dirac points can occur along these high-symmetry lines. Thus the symmetry-enforced Dirac points can only occur along the high-symmetry lines DT and P.

It has been demonstrated that 3D DSMs can host 1D HOFAs on hinges [11, 13, 26]. The HOFAs can be interpreted by the nontrivial filling anomaly η for a symmetrically terminated 2D insulating planes with fixed $k_z \neq 0, \pi$ between the symmetry-enforced Dirac points. In the presence of six-fold rotational symmetry, we can always consider a regular hexagon 2D plane with fixed k_z . Since the termination dependence of the edge BZ, the armchair-terminated edge would lead to the absence of HOFAs due to the zone-folding effects [9, 44]. Thus the finite-sized rod discussed in this paper is zigzag-terminated and the edge lattice vectors are the same as the bulk lattice vectors.

When the filling anomaly η is nonzero, the finite 2D insulating plane cannot keep both neutral and symmetrical, which means that the mid-gap states must occur. Furthermore, if the finite 2D insulating plane has no polarization (boundary charge), the mid-gap states must be localized at the corners, which leads to the HOFA states. Two possible kinds of topological phases are related to filling anomalies, i.e., obstructed atomic limit phases [13, 15, 30, 45] and fragile topological

TABLE I. The elementary band representations (EBRs) induced into Type-II SSG $P6/mmm1'$ from the double-valued site symmetry representations at the $1a$ Wyckoff Position, and the subduced little group representations at Γ .

Site-Symmetry Representation	Spinful Atomic Orbitals	Small Coreps Subduced at Γ
$(\bar{E}_{1g})_{1a}$	s	$\bar{\Gamma}_9$
$(\bar{E}_{1u})_{1a}$	f -orbital related	$\bar{\Gamma}_{12}$
$(\bar{E}_{2g})_{1a}$	d -orbital related	$\bar{\Gamma}_8$
$(\bar{E}_{2u})_{1a}$	p_z	$\bar{\Gamma}_{11}$
$(\bar{E}_{3g})_{1a}$	d -orbital related	$\bar{\Gamma}_7$
$(\bar{E}_{3u})_{1a}$	p -orbital related	$\bar{\Gamma}_{10}$

phases [9, 46–48]. Obstructed atomic limit phases are Wannierizable, whose filling anomalies are determined by the number of Wannier centers at each Wyckoff position; Fragile phases are non-Wannierizable but can be viewed as a subtraction between two atomic limit phases, such that filling anomalies are also well-defined. As a result, HOFA states can stem from either obstructed atomic limit phases or fragile topological phases with nontrivial filling anomalies.

The filling anomaly η can be calculated by using the theories of band representations and symmetry-based indicators (SIs) established in MTQC. In these theories, electronic BSs can be represented by symmetry data vectors \mathbf{B} of occupied bands, i.e., $\{\text{BS}\} = \{\mathbf{B}\}$. For an insulating system, the mismatch between the possible atomic limit insulators and the symmetry data vector \mathbf{B} leads to a topological (crystalline) insulator. Such that the symmetry group for an insulator can be given by the quotient group [33]:

$$X_{\text{BS}} \equiv \frac{\{\text{BS}\}}{\{\text{AI}\}}, \quad (4)$$

where

$$\{\text{AI}\} = \left\{ \sum_j l_j \mathbf{a}_i | l_j \in \mathbb{Z} \right\} \quad (5)$$

is the set of symmetry data of atomic limit insulators. Here \mathbf{a}_i are the atomic limit elementary band representations (EBRs) which compose a complete set of $\{\text{AI}\}$. We list part of the information of the EBRs in Tab. I, while the full EBRs of Type-II double SSG $P6/mmm1'$ are listed in Supplementary Note 1. For a certain (magnetic) space group, the symmetry group takes the form $X_{\text{BS}} = \mathbb{Z}_{n_1} \times \mathbb{Z}_{n_2} \times \dots$, which can be calculated by the Smith normal decomposition of $\{\text{AI}\}$.

For DSMs respecting the symmetries of Type-II double SSG $P6/mmm1'$, the 2D planes with fixed $k_z \neq 0, \pi$ respect the symmetries of Type-III MLG $p6/m'mm$, while the 2D planes with $k_z = 0, \pi$ respect the

symmetries of Type-II SLG $p6/mmm1'$. The boundary charge of the 2D planes can be determined by the double SIs, which are also called the stable topological indices (see Supplementary Notes 2 and 3). When the double SIs vanish, the 2D systems do not host stable topological phases and are in either (possibly obstructed) atomic limit or fragile phases. The 2D filling anomaly is given by [11, 13]

$$\eta = a_a - e_a \pmod{6 \text{ or } 12}, \quad (6)$$

where a_a and e_a are the numbers of atoms and electron Wannier centers at the Wyckoff position $1a$, respectively. By definition, $e_a \equiv \sum_{\rho_a} n_{\rho_a} \dim(\rho_a)$ with ρ_a being the representations of the electron Wannier functions centered at the Wyckoff position $1a$, and the operator $\dim(\rho_a)$ gives the dimension of ρ_a . We denote the number of the electron Wannier representations ρ_a by n_{ρ_a} . The modulo 6 or 12 depends on whether the time-reversal symmetry is absent or not. Through the EBR analysis, the 2D filling anomaly can be expressed in terms of the multiplicities of double-valued small coreps of little co-groups. Here we summarize the main results while the detailed calculations of the symmetry group for $p6/m'mm$ and $p6/mmm1'$ are specifically shown in Supplementary Notes 2 and 3.

(1) Type-III MLG $p6/m'mm$. The SI group of $G = p6/m'mm$ is $X_{\text{BS}} = \mathbb{Z}_1$, which means that there are no symmetry-based indicators, i.e., no stable topological phases exist. The filling anomaly is given by Eq. 6 with

$$n_a = m(\bar{\Gamma}_8) + m(\bar{\Gamma}_9) + m(\bar{K}_4\bar{K}_5) \pmod{6}, \quad (7)$$

where $m(u_{\mathbf{k}}^\alpha)$ is the multiplicity of α^{th} small corep of the little co-groups $G_{\mathbf{k}}$ listed in Table II. Ref. [11] proved that the HOFA states can be indicated by the relative topology across the Dirac points, which can be given by the change in the filling anomaly

$$\begin{aligned} \Delta\eta &= -2\Delta n_a \\ &= -2(\Delta m(\bar{\Gamma}_8) + \Delta m(\bar{\Gamma}_9) + \Delta m(\bar{K}_4\bar{K}_5)) \pmod{6}. \end{aligned} \quad (8)$$

where $\Delta m(u_{\mathbf{k}}^\alpha)$ can be determined by the change in the subduced small coreps of the valence bands. For example, Eq. 2 leads to the change in the symmetry data vector

$$\begin{aligned} \Delta\mathbf{B} &= \mathbf{B}(k_0 + \delta k_z) - \mathbf{B}(k_0 - \delta k_z) \\ &= (1, 0, -1, 0, 0, 0). \end{aligned} \quad (9)$$

The relative topology is nontrivial with $\Delta\eta = \eta(\Delta\mathbf{B}) = 2$, which indicates the presence of HOFA states.

(2) Type-II SLG $p6/mmm1'$. The SI group of $G = p6/mmm1'$ is $X_{\text{BS}} = \mathbb{Z}_6$, The SI is given by

$$\begin{aligned} z_6(\mathbf{B}) &= -m(\bar{\Gamma}_7) + m(\bar{\Gamma}_8) + 3m(\bar{\Gamma}_9) \\ &\quad + 2m(\bar{\Gamma}_{10}) - 2m(\bar{\Gamma}_{12}) - 2m(\bar{K}_7) \\ &\quad + 2m(\bar{K}_8) - 3m(\bar{M}_5) \pmod{6}, \end{aligned} \quad (10)$$

which is also the mirror Chern number. When the $z_6 = 0$, the filling anomaly is well defined and is given by Eq. 6 with

$$\begin{aligned} n_a &= \frac{11}{2}m(\bar{\Gamma}_7) - \frac{9}{2}m(\bar{\Gamma}_8) - \frac{1}{2}m(\bar{\Gamma}_9) \\ &\quad + 7m(\bar{\Gamma}_{10}) + m(\bar{\Gamma}_{11}) - 3m(\bar{\Gamma}_{12}) \\ &\quad - 6m(\bar{K}_7) + 4m(\bar{K}_8) + \frac{3}{2}m(\bar{M}_5) \pmod{12}. \end{aligned} \quad (11)$$

The small coreps of the little co-groups $G_{\mathbf{k}}$ are also listed in Table II. Similar to Eq. 8, the relative topology can be defined between the two TRIM planes with $k_z = 0, \pi$. Such that the change in the symmetry data vector is

$$\Delta\mathbf{B} = \mathbf{B}(\pi) - \mathbf{B}(0). \quad (12)$$

Thus the change in the filling anomaly is also given by $\Delta\eta = \eta(\Delta\mathbf{B})$.

TABLE II. (Magnetic) little co-groups of Type-III MLG $p6/m'mm$ and Type-II SLG $p6/mmm1'$ at the high symmetry points $\mathbf{k}_\Gamma = (0, 0)$, $\mathbf{k}_K = (1/3, 1/3)$, and $\mathbf{k}_M = (1/2, 0)$.

	Γ	K	M
$p6/m'mm$	$6/m'mm$	$3'm$	$m'mm$
$p6/mmm1'$	$6/mmm1'$	$6'/mm'm$	$mmm1'$

III. NODAL DIRAC SUPERCONDUCTING STATE WITH HOTDSC STATES

In this section, we will focus on possible nodal Dirac superconducting states from Dirac semimetals respecting Type-II SSG $P6/mmm1'$ discussed above. We restrict our discussion to superconductors described by the Bardeen-Cooper-Schrieffer theory. Similar to the topological (crystalline) insulators and semimetals, superconducting BSs can also be described by the band representation theory. However, the conventional SIs are not enough to distinguish all topologically nontrivial superconducting states, such as the 1D Kitaev chain and HOTDSCs. Thus the refined SIs have been proposed as a reliable method to identify TSCs [37]. The refined symmetry groups for superconductors are given by

$$X^{\text{BdG}} \equiv \frac{\{\text{BS}\}^{\text{BdG}}}{\{\text{AI}\}^{\text{BdG}}}, \quad (13)$$

where $\{\text{BS}\}^{\text{BdG}} = \{\mathbf{B}^{\text{BdG}} - \mathbf{B}^{\text{vac}}\}$ is the set of all possible $\mathbf{B}^{\text{BdG}} - \mathbf{B}^{\text{vac}}$. Here \mathbf{B}^{BdG} is the symmetry data vector of all the bands with $E < 0$ of the BdG Hamiltonian; \mathbf{B}^{vac} is the symmetry data vector of all the bands with $E < 0$ of the corresponding trivial BdG

TABLE III. Character table for the D_{6h} point group.

Matrix	Symmetry operators		
	$\{6_{001}^+ \mathbf{0}\}$	$\{\bar{1} \mathbf{0}\}$	$\{2_{110} \mathbf{0}\}$
A_{1g}	1	1	1
A_{2g}	1	1	-1
B_{1g}	-1	1	1
B_{2g}	-1	1	-1
A_{1u}	1	-1	1
A_{2u}	1	-1	-1
B_{1u}	-1	-1	1
B_{2u}	-1	-1	-1

Hamiltonian. The atomic limit of the BdG system is given by the set

$$\{\text{AI}\}^{\text{BdG}} = \left\{ \sum_j l_j (\mathbf{a}_i - \bar{\mathbf{a}}_i) | l_j \in \mathbb{Z} \right\}, \quad (14)$$

where \mathbf{a}_i is the atomic limit EBR used in the case of normal states, $\bar{\mathbf{a}}_i$ is the EBR which is related to \mathbf{a}_i by the particle-hole symmetry \mathcal{P} in a specific pairing representation. Given that the corresponding point group is D_{6h} ($6/mmm$) for Type-II SSG $P6/mmm1'$, there are eight real 1D representations, i.e., A_{1g} , A_{2g} , A_{1u} , A_{2u} , B_{1g} , B_{2g} , B_{1u} , and B_{2u} . These representations are distinguished by their characters $\chi_{\{6_{001}^+|\mathbf{0}\}}$, $\chi_{\{\bar{1}|\mathbf{0}\}}$, and $\chi_{\{2_{110}|\mathbf{0}\}}$ (see Table III). Since the small coreps at the high-symmetry points in the BZ are not distinguished by $\chi_{\{2_{110}|\mathbf{0}\}}$, the pairing representations with the same $\chi_{\{6_{001}^+|\mathbf{0}\}}$ and $\chi_{\{\bar{1}|\mathbf{0}\}}$ will share the same topological classification in refined SI groups. Thus we can discuss the topological (crystalline) superconducting phases in A_{1g}/A_{2g} , A_{1u}/A_{2u} , B_{1g}/B_{2g} , and B_{1u}/B_{2u} pairing channels, respectively.

Apart from refined SIs, HOTDSC states can also be indicated by 2D filling anomalies of gapped BdG systems similar to Eq. 6 for normal states, which is given by

$$\eta^{\text{BdG}} = \eta + \eta' \quad (15)$$

where η' is filling anomaly of the BdG shadow Hamiltonian $\mathcal{P}H(\mathbf{k})\mathcal{P}^{-1} = -H^*(-\mathbf{k})$. In practice, if the eigenstates of $H_{\mathbf{k}}$ are $\Psi_{\mathbf{k}}$ which belongs to an irrep $u_{\mathbf{k}}^\alpha$ of the little group $G_{\mathbf{k}}$, we can get that the irrep of eigenstates the corresponding BdG shadow Hamiltonian is $\chi_g(u_{\mathbf{k}}^\alpha)^*$ of $G_{-\mathbf{k}}$. Thus we can obtain the symmetry data vector \mathbf{B}' of the BdG shadow Hamiltonian when the symmetry data vector \mathbf{B} of the normal state and the characters χ_g of the pairing channel are known. The value of the nontrivial BdG filling anomaly corresponds to the number of Majorana zero modes (MZMs) at corners. Since the MZMs are neutral excitations consisting of an equal superposition of electrons and holes, the filling anomaly of the normal state and that of the corresponding BdG shadow states should satisfy $\eta = \eta'$.

To discuss the possible nodal topological superconducting states in Dirac semimetals, we

may first use the compatibility relations to determine whether the BdG Dirac points will occur along the high-symmetry lines. Similar to the discussion in normal states, BdG Dirac points occur when small coreps cross. However, since the particle-hole symmetry will double the number of the bands, the BdG Dirac points are not all symmetry-enforced, i.e., some of the BdG Dirac points can be gapped without breaking any symmetry which we term the (accidental) non-symmetry-enforced BdG Dirac points. This kind of BdG Dirac points arise from identical small coreps and the topological states will not be changed across this kind of BdG Dirac points. Instead, symmetry-enforced BdG Dirac points arise from the crossing of distinct small coreps such that they would lead to the nontrivial relative topology.

As discussed in the previous section, the symmetry-enforced bulk Dirac points of the normal states can occur along DT and P. For the former case, since there are only 3 different small coreps at DT but there are four bands in the superconducting BS, there at least two bands with the same small coreps at DT. Thus only one of the BdG Dirac points is symmetry-enforced. For the latter case, since there are 2 different small coreps along P in the four bands, there are no symmetry-enforced BdG Dirac points inherited from the Dirac points in normal states. Thus in the following discussion, we will focus on the nodal Dirac superconducting states from Dirac semimetals with Dirac points along DT.

We take the superconducting states in Dirac semimetals with subduced small coreps $\bar{\Gamma}_9$ and $\bar{\Gamma}_{10}$ at the high-symmetry point Γ as an example. When the superconducting pairing representations are B_{1u}/B_{2u} , another two bands with small coreps $\bar{\Gamma}_7$ and $\bar{\Gamma}_{11}$ will be added into the BdG BS owing to the particle-hole symmetry, as shown in Fig. 3. The compatibility relations in Eq. 1 imply that $\bar{\Gamma}_{10}$ and $\bar{\Gamma}_7$ are both connected to $\overline{\text{DT}}_7$, such that there are two kinds of possible BdG Dirac points in this system. The non-symmetry-enforced BdG Dirac points arise from the two $\overline{\text{DT}}_7$ crossing in the BS such that the relative topology is trivial (see the blue dot in Fig. 3). While the symmetry-enforced BdG Dirac points arise from the crossing of $\overline{\text{DT}}_8$ and $\overline{\text{DT}}_9$ (see the red dots in Fig. 3). Thus the topological properties of the 2D planes with fixed k_z will be changed across the symmetry-enforced BdG Dirac point, which can be indicated by the nontrivial relative topology.

For the 2D planes with $k_z \neq 0, \pi$, the magnetic layer group is $p6/m'mm$. Although the symmetry-enforced BdG Dirac points occur, given that all the refined SIs vanish (see Supplementary Note 7), we deduce that there are no topological superconducting states in these 2D planes. Thus there are no HOMA states in superconductors respecting Type-II SSG $P6/mmm1'$.

The symmetry-enforced BdG Dirac points can also lead to the nontrivial relative topology between the two TRIM planes. The 2D TRIM planes with $k_z = 0, \pi$ both respect the symmetries of Type-II SLG $p6/mmm1'$. As shown in Fig. 3, the 2D superconducting phases would

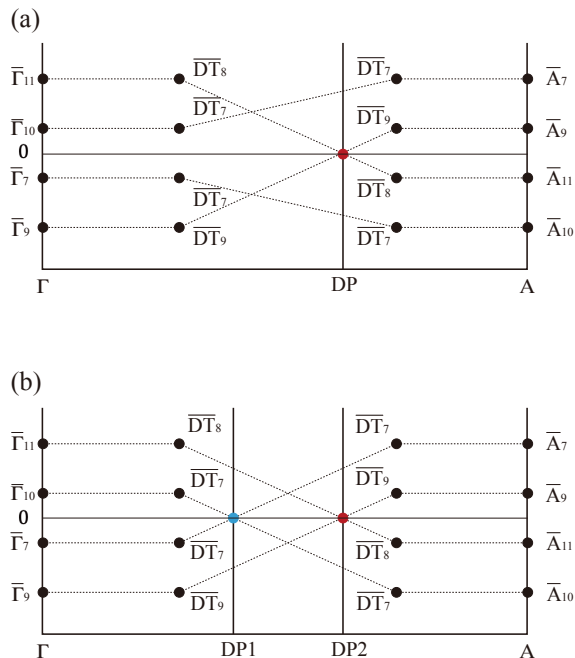


FIG. 3. Compatibility relations of the co-representations of a nodal Dirac superconducting system respecting Type-II SSG $P6/mmm1'$. (a) There is only one symmetry-enforced BdG Dirac point (red dot) following the compatibility relations. (b) Because of the particle hole symmetry, there can be a non-symmetry-enforced BdG Dirac points (blue dot) occurring along DT, but it will not leads to nontrivial relative topology.

inherit the change in the valence small coreps at Γ in the BZ of Type-II SLG $p6/mmm1'$ when we turn $k_z = 0$ to $k_z = \pi$, i.e., $\bar{\Gamma}_9 \rightarrow \bar{\Gamma}_{10}$. Additionally, since the normal state is half-filling, the particle-hole symmetry and the superconducting pairing representations B_{1u}/B_{2u} would lead to another valence change $\bar{\Gamma}_7 \rightarrow \bar{\Gamma}_{11}$ in the corresponding BdG shadow states. Thus when we turn $k_z = 0$ to $k_z = \pi$, the total valence exchanges arising from the symmetry-enforced Dirac point are

$$\bar{\Gamma}_9 \rightarrow \bar{\Gamma}_{10}, \quad (16)$$

$$\bar{\Gamma}_7 \rightarrow \bar{\Gamma}_{11}, \quad (17)$$

The symmetry data vector of the BdG system can be given by the summation $\mathbf{B}^{\text{BdG}} = \mathbf{B} + \mathbf{B}'$, where \mathbf{B} and \mathbf{B}' are the symmetry data vectors of the normal state and the corresponding BdG shadow state, respectively. The change in BdG symmetry data vector can be written as

$$\begin{aligned} \Delta \mathbf{B}^{\text{BdG}} &= \Delta \mathbf{B} + \Delta \mathbf{B}' \\ &= (-1, 0, -1, 1, 1, 0, 0, 0, 0, 0). \end{aligned} \quad (18)$$

Moreover, the change in the conventional SIs can be calculated by

$$\Delta z_6 = z_6(\Delta \mathbf{B}^{\text{BdG}}) = 0 \pmod{6}. \quad (19)$$

We note that $\Delta z_6 = 0$ does not always imply that the topological superconducting phases of the two TRIM planes are the same. This argument can be verified by the further calculation of the difference of the refined SIs. For the B_{1u}/B_{2u} superconducting pairing representations, the refined symmetry group is \mathbb{Z}_4 (see Supplementary Note 6). We can obtain the change in the refined SIs by

$$\Delta z_4 = z_4(\Delta \mathbf{B}^{\text{BdG}}) = 2 \pmod{4}. \quad (20)$$

The nonzero value of Δz_4 demonstrates that the TRIM planes with $k_z = 0, \pi$ indeed exhibit different topological phases. Moreover, the change in BdG filling anomalies is given by

$$\Delta \eta^{\text{BdG}} = -2n_a(\Delta \mathbf{B}^{\text{BdG}}) = -6 \pmod{24} \quad (21)$$

The integer value of $\Delta \eta^{\text{BdG}}$ shows that when one of the TRIM planes is topologically trivial with $\eta^{\text{BdG}} = 0$, another TRIM plane must show the nontrivial filling anomaly $|\eta^{\text{BdG}}| = 6$, indicating the presence of 6 Kramer pairs of Majorana zero modes (MZMs) at the 6 corners. Thus Eq. 21 can be viewed as the topological charge of the symmetry-enforced BdG Dirac points. We can verify this argument by the numerical calculation of the tight-binding models in Sec. IV.

Furthermore, we have calculated the relative topologies in all possible BSs of Dirac semimetals respecting Type-II SSG $P6/mmm1'$ and tabulated the results in Supplementary Note 8. We find that for symmetry-enforced nodal Dirac superconducting states, $|\Delta \eta^{\text{BdG}}| = 6$ can only occur in DSMs with HOFA states with the B_{1u}/B_{2u} superconducting pairing representations.

We note that three kinds of changes in the small coreps of valence bands in normal states $\bar{\Gamma}_7 \rightarrow \bar{\Gamma}_{10}$, $\bar{\Gamma}_8 \rightarrow \bar{\Gamma}_{11}$, and $\bar{\Gamma}_9 \rightarrow \bar{\Gamma}_{12}$ would not lead to symmetry-enforced DSMs since the small coreps along DT are the same in the deformation of k_z . Thus their superconducting states can not host symmetry-enforced BdG Dirac points but can host accidental Dirac crossings instead. However, the absence of symmetry-enforced BdG Dirac points does not mean the absence of HOTDSC states. In Supplementary Note 8, we find that superconducting states without symmetry-enforced BdG Dirac points can still host HOTDSC states on the TRIM planes, which can also be identified by relative topologies. For example, the superconducting states in DSMs with $\bar{\Gamma}_8 \rightarrow \bar{\Gamma}_{12}$ can not host symmetry-enforced BdG Dirac points but exhibit HOTDSC states on TRIM planes in the B_{1u}/B_{2u} or A_{1u}/A_{2u} pairing channels; The superconducting states in topological insulators with $\bar{\Gamma}_7 \rightarrow \bar{\Gamma}_{10}$ can host neither symmetry-enforced Dirac points nor the symmetry-enforced BdG Dirac points but also exhibit HOTDSC states on TRIM planes in the B_{1u}/B_{2u} or A_{1u}/A_{2u} pairing channels.

IV. TIGHT-BINDING MODEL

A. Normal state

In this section, we will discuss the possible topological superconducting phases in DSMs respecting the symmetries of Type-II SG $P6/mmm1'$ by specific tight-binding models. To be consistent with the previous sections, we begin with an $s-p_z$ hybridized HOFA Dirac semimetals with subduced small coreps $\bar{\Gamma}_9$ and $\bar{\Gamma}_{10}$ at the high-symmetry point Γ as an example. In this way, the Dirac points can occur along the high-symmetry lines DT or P, depending on the values of the parameters. Following the irreps of the symmetry operators in $\bar{\Gamma}_9$ and $\bar{\Gamma}_{10}$, the matrix forms of the generators of Type-II SPG $6/mmm1'$ are given by

$$\{6_{001}^+|\mathbf{0}\} = \begin{pmatrix} e^{i\pi/6} & & & \\ & e^{-i\pi/6} & & \\ & & -i & \\ & & & i \end{pmatrix}, \quad (22)$$

$$\{2_{110}|\mathbf{0}\} = \begin{pmatrix} & -1 & & \\ 1 & & & \\ & & -1 & \\ & & & 1 \end{pmatrix}, \quad (23)$$

$$\{\bar{1}|\mathbf{0}\} = \begin{pmatrix} 1 & & & \\ & 1 & & \\ & & -1 & \\ & & & -1 \end{pmatrix}, \quad (24)$$

$$\{1'|\mathbf{0}\} = \begin{pmatrix} & 1 & & \\ -1 & & & \\ & & -1 & \\ & & & 1 \end{pmatrix} \mathcal{K}, \quad (25)$$

where we have adopted the symmetry notations in BCS [42, 43]. Combining the 3D lattice translation symmetries $\{E|100\}$, $\{E|010\}$, and $\{E|001\}$, we can generate a continuous DSM Hamiltonian respecting the symmetries of Type-II MSG $P6/mmm1'$ with SOC by the Qsymm software package [49]:

$$\begin{aligned} \mathcal{H}_{\mathbf{k}} = & [m_1 + m_2 (k_x^2 + k_y^2) + m_3 k_z^2] \sigma_z s_0 \\ & + A_1 k_x (\sigma_y s_y - \sqrt{3} \sigma_y s_x) \\ & - A_1 k_y (\sqrt{3} \sigma_y s_y + \sigma_y s_x) \\ & + A_2 (k_x^3 + k_x k_y^2) (\sigma_y s_y - \sqrt{3} \sigma_y s_x) \\ & - A_2 (k_y^3 + k_x^2 k_y) (\sqrt{3} \sigma_y s_y + \sigma_y s_x) \\ & + 2B k_x k_y k_z (\sigma_x s_0 - \sqrt{3} \sigma_y s_z) \\ & + B (k_x^2 - k_y^2) k_z (\sqrt{3} \sigma_x s_0 + \sigma_y s_z), \end{aligned} \quad (26)$$

where σ (s) indexes the s , p_z -orbital (spin) degree of freedom. This four-band $k.p$ model is equivalent to that

introduced in Ref. [11] connecting to Na_3Bi . The total power of the momentum variables is up to 3. This model can be extended to a tight-binding model, which is given by

$$\begin{aligned} \mathcal{H}_{\mathbf{k}} = & (\tilde{M}_0 + 2\tilde{M}_1 \cos k_z) \sigma_z s_0 \\ & + 2\tilde{M}_2 \left(2 \cos \frac{k_x}{2} \cos \frac{\sqrt{3}k_y}{2} + \cos k_x \right) \sigma_z s_0 \\ & + 2\tilde{A} \left(\sin \frac{k_x}{2} \cos \frac{\sqrt{3}k_y}{2} + \sin k_x \right) (\sigma_y s_y - \sqrt{3} \sigma_y s_x) \\ & - 2\tilde{A} \left(\sqrt{3} \cos \frac{k_x}{2} \sin \frac{\sqrt{3}k_y}{2} \right) (\sqrt{3} \sigma_y s_y + \sigma_y s_x) \\ & + 2\tilde{B} \sqrt{3} \sin k_z \sin \frac{k_x}{2} \sin \frac{\sqrt{3}k_y}{2} (\sigma_x s_0 - \sqrt{3} \sigma_y s_z) \\ & - 2\tilde{B} \sin k_z \left(\cos k_x - \cos \frac{k_x}{2} \cos \frac{\sqrt{3}k_y}{2} \right) \\ & \times (\sqrt{3} \sigma_x s_0 + \sigma_y s_z). \end{aligned} \quad (27)$$

To obtain the parameter conditions for the presence of Dirac crossings along the high-symmetry lines DT or P, we can first obtain the corresponding energy of the double-valued small coreps at Γ , A , K , and H :

$$E(\bar{\Gamma}_9) = -E(\bar{\Gamma}_{10}) = \tilde{M}_0 + 2\tilde{M}_1 + 6\tilde{M}_2, \quad (28)$$

$$E(\bar{A}_9) = -E(\bar{A}_{10}) = \tilde{M}_0 - 2\tilde{M}_1 + 6\tilde{M}_2, \quad (29)$$

$$E(\bar{K}_7) = -E(\bar{K}_9) = -\tilde{M}_0 - 2\tilde{M}_1 + 3\tilde{M}_2, \quad (30)$$

$$E(\bar{H}_7) = -E(\bar{H}_9) = -\tilde{M}_0 + 2\tilde{M}_1 + 3\tilde{M}_2. \quad (31)$$

If the Dirac crossings occur along DT, the energies of the Bloch states should satisfy $E(\bar{\Gamma}_9) \cdot E(\bar{A}_9) < 0$, i.e., the parameter condition for the occurrence of Dirac points along DT is

$$|\tilde{M}_0 + 6\tilde{M}_2| < 2|\tilde{M}_1|. \quad (32)$$

Similarly, if the Dirac crossings occur along P, the energy of the Bloch states should satisfy $E(\bar{K}_9) \cdot E(\bar{H}_9) < 0$, i.e., the parameter condition for the occurrence of the Dirac points along P is

$$|\tilde{M}_0 - 3\tilde{M}_2| < 2|\tilde{M}_1|. \quad (33)$$

In this work, we will take the parameters in Tab. IV and restrict our discussion to the Dirac points occurring along the high-symmetry line DT in Fig. 1. As shown in Fig. 2, the small coreps of the valence Bloch states ($\zeta_{\mathbf{k}}$) and the conducting Bloch states ($\bar{\zeta}_{\mathbf{k}}$) at Γ and DT with $\mathbf{k}_0 - \delta k_z$ are given by

$$\zeta_{\Gamma} = \bar{\Gamma}_9, \quad (34)$$

$$\bar{\zeta}_{\Gamma} = \bar{\Gamma}_{10}, \quad (35)$$

$$\zeta_{\mathbf{k}_0 - \delta k_z} = \bar{\text{DT}}_9, \quad (36)$$

$$\bar{\zeta}_{\mathbf{k}_0 - \delta k_z} = \bar{\text{DT}}_7, \quad (37)$$

TABLE IV. Tight-binding parameters.

\tilde{M}_0	\tilde{M}_1	\tilde{M}_2	\tilde{A}	\tilde{B}
4	-1.5	-1	1	5

where δk_z is a small and positive momentum. Similarly, the representations of the Bloch states at A and DT with $\mathbf{k}_0 + \delta k_z$ are given by

$$\zeta_A = \bar{A}_{10}, \quad (38)$$

$$\bar{\zeta}_A = \bar{A}_9, \quad (39)$$

$$\zeta_{\mathbf{k}_0 + \delta k_z} = \bar{D}\bar{T}_7, \quad (40)$$

$$\bar{\zeta}_{\mathbf{k}_0 + \delta k_z} = \bar{D}\bar{T}_9. \quad (41)$$

Thus we can obtain the symmetry data vectors for the 2D planes at $k_z = 0, \pi, k_0 - \delta k_z$, and $k_0 + \delta k_z$, respectively:

$$\mathbf{B}(0) = (0, 0, 1, 0, 0, 0, 1, 0, 0, 0, 1), \quad (42)$$

$$\mathbf{B}(\pi) = (0, 0, 0, 1, 0, 0, 1, 0, 0, 0, 1), \quad (43)$$

$$\mathbf{B}(k_0 - \delta k_z) = (0, 0, 1, 1, 0, 1), \quad (44)$$

$$\mathbf{B}(k_0 + \delta k_z) = (1, 0, 0, 1, 0, 1), \quad (45)$$

which indicates a Dirac crossing along DT in Fig. 4(a).

We now discuss the topological properties in the 2D momentum slices with fixed k_z . When $k_z = 0$ and π , the 2D slices respect the symmetries of Type-II SLG $p6/mmm1'$, which can be indicated by the \mathbb{Z}_6 -valued double SI (see Supplementary Note 2 for details). Employing symmetry data vectors listed in Eqs. 42 and 43, we can obtain the stable topological indices in Eq. 10 for the planes with $k_z = 0$ and π are $z_6 = 1$ and 0, respectively. These are also the mirror Chern numbers. The nonzero-valued z_6 for the plane at $k_z = 0$ indicates a TCI state whose symmetry data vector cannot be written purely as a linear combination (sum or difference) of EBRs, i.e.,

$$\exists \mathbf{p} = (p_1, p_2, \dots)^T \notin \mathbb{N}^{N_{\text{EBR}}}, \text{ s.t. } \mathbf{B} = \mathcal{E}\mathcal{B}\mathcal{R} \cdot \mathbf{p}, \quad (46)$$

where N_{EBR} is the number of EBRs in the (magnetic) space group. In this tight-binding model, the combination vector \mathbf{p} is given by

$$\mathbf{p} = \left(-\frac{1}{2}, 0, -\frac{1}{2}, \frac{1}{2}, 0, 0, 0, 0, \frac{1}{2}, 0 \right) \text{ mod } 2. \quad (47)$$

The fractional combination vector \mathbf{p} is a hallmark of stable topological surface phases, as shown in Fig. 4(b).

For the planes at $k_z \neq 0, \pi$, the 2D planes respecting the symmetries of Type-III MLG $p6/m'mm$, all the stable topological indices vanish. By using the symmetry data vectors in Eqs. 44, 45 and the formula in Eq. 6, we can calculate the filling anomaly of the planes at $k_0 \pm \delta k_z$. Specifically, we can obtain $\eta = -2$ for the planes at $k_0 - \delta k_z$ and $\eta = 0$ for the planes at $k_0 + \delta k_z$. As shown in Figs. 4(c)-(e), we can see that the HOFAs occur between

$k_z = 0$ and k_0 . Thus the presence of HOFAs can be indicated by the change in the filling anomaly $\Delta\eta = 2$, consistent with our discussion in Sec. II. This result has been demonstrated in Ref. [11].

In Fig. 4(f), we show the Wilson spectra computed from the pairs valence bands in Fig. 4(b), which shows trivial winding. Thus the valence bands are ‘‘Wannier-representable’’, i.e., the corresponding Wannier functions are exponentially localized and respect all the symmetries of Type-III MLG $p6/m'mm$. These planes can be regarded as 2D obstructed atomic insulators (OAI). The Dirac points can be viewed as the critical points between the obstructed atomic insulators and trivial phases. Such that the Dirac points can be classified by the change in the filling anomaly [11].

One might expect similar critical points occurring in BdG system, which leads to HOMAs as those in Ref. [26]. However, we have demonstrated that the HOMAs cannot occur in DSMs respecting the symmetry of Type-II MSG $P6/mmm1'$ due to the trivial BdG refined SIs at the planes with $k_z \neq 0, \pi$ (see Supplementary Note 7). Instead, the HOFAs in normal states can only lead to higher-order Majorana zero modes at TRIM planes in B_{1u}/B_{2u} pairing channels. We will show that the topological properties of superconducting systems with symmetry-enforced BdG Dirac points can also be identified by the relative topology.

B. Superconducting states with B_{1u}/B_{2u} pairings

For a superconducting system respecting Type-II SSG $P6/mmm1'$, the intrinsic particle-hole symmetry satisfies $\mathcal{P}^2 = +\xi$ and $\xi = \pm 1$. The superconducting systems fall into class DIII (if $\xi = +1$) or CII (if $\xi = -1$). Given that it is difficult to construct class CII electronic systems in experiments, we will focus on the superconducting systems in class DIII. For clarity, we rewrite the BdG Hamiltonian in the following form:

$$\mathcal{H}_k^{\text{BdG}} = \mathcal{H}_0 + \mathcal{H}_\Delta, \quad (48)$$

$$\mathcal{H}_0 = \begin{pmatrix} \mathcal{H}_k & \\ & -\mathcal{H}_{-\mathbf{k}}^* \end{pmatrix}, \quad (49)$$

$$\mathcal{H}_\Delta = \begin{pmatrix} & \Delta_{\mathbf{k}} \\ \Delta_{\mathbf{k}}^\dagger & \end{pmatrix}. \quad (50)$$

where \mathcal{H}_k is the Hamiltonian of normal states. The superconducting pairing potential \mathcal{H}_Δ can be obtained from the eight 1D real pairing representations of Type-II SSG $P6/mmm1'$. As discussed in Sec. III, for symmetry-enforced nodal Dirac superconducting states, the higher-order topological superconducting states can only occur in HOFAs normal states with B_{1u}/B_{2u} pairings. To numerically verify this conclusion, we first obtain the matrix form of any spatial symmetry operator g in BdG Hamiltonian

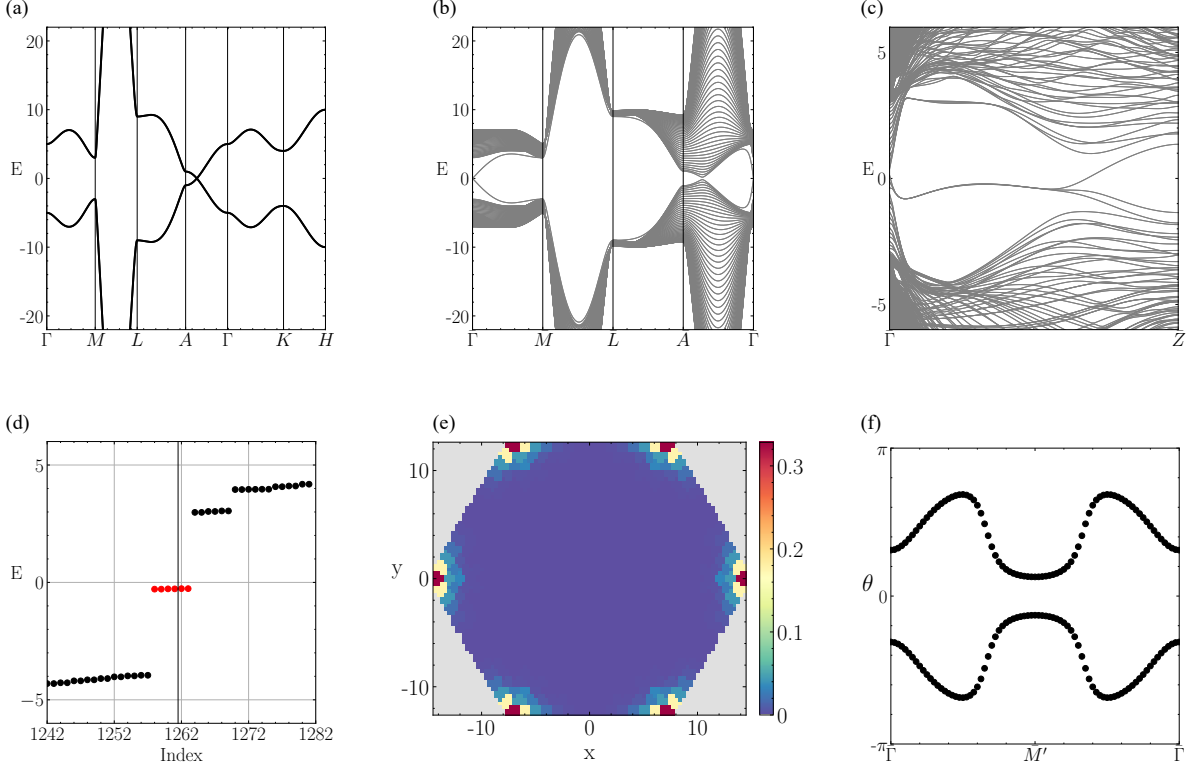


FIG. 4. (a) Bulk spectrum of the tight-binding model Eq. 27. (b) Surface spectrum of the tight-binding model in ribbon geometry when we terminate the 3D lattice in the a_2 direction. (c) Rod spectrum of the tight-binding model when we terminate the 3D lattice in the a_1 and a_2 directions. (d) Energy of the states at $k_z = \pi/4$ of the tight-binding model in rod geometry. The red dots are the corner states composing the HOFAs. (e) Wave-function distribution of the mid-gap states (red dots in (d)) at $k_z = \pi/4$. (f) a_2 -directed Wilson loops at $k_z = \pi/4$ plotted as functions of k_{b_1} . All the figures are computed by the PythTb [50] and Kwant [51] software packages.

$$U_{\mathbf{k}}^{\text{BdG}}(g) \equiv \begin{pmatrix} U_{\mathbf{k}}(g) & \\ & \chi_g U_{-\mathbf{k}}^*(g) \end{pmatrix}, \quad (51)$$

where χ_g is the character of the corresponding pairing representation, as shown in Table III. The unitary matrix $U_{\mathbf{k}}(g)$ is the matrix representation of each element g in the spatial little group at \mathbf{k} and satisfies

$$U_{\mathbf{k}}(g) \mathcal{H}_{\mathbf{k}} U_{\mathbf{k}}^\dagger(g) = \mathcal{H}_{g\mathbf{k}}. \quad (52)$$

Such that any spatial symmetry operator in a BdG system satisfies

$$U_{\mathbf{k}}^{\text{BdG}}(g) \mathcal{H}_{\mathbf{k}}^{\text{BdG}} U_{\mathbf{k}}^{\text{BdG}\dagger}(g) = \mathcal{H}_{g\mathbf{k}}^{\text{BdG}}. \quad (53)$$

When the time-reversal symmetry is preserved in a BdG system, the Hamiltonian should satisfy

$$U_{\mathcal{T}} \mathcal{H}_{\mathbf{k}}^* U_{\mathcal{T}}^\dagger = \mathcal{H}_{-\mathbf{k}}, \quad (54)$$

$$U_{\mathcal{T}} \Delta_{\mathbf{k}}^* U_{\mathcal{T}}^\dagger = \Delta_{-\mathbf{k}}. \quad (55)$$

Thus the time-reversal symmetry takes the matrix form

$$U_{\mathcal{T}}^{\text{BdG}} \equiv \begin{pmatrix} U_{\mathcal{T}} & \\ & U_{\mathcal{T}}^* \end{pmatrix}. \quad (56)$$

For B_{1u}/B_{2u} pairings, the characters are $\chi_{\{6_{001}^+|\mathbf{0}\}} = -1$ and $\chi_{\{\bar{1}|\mathbf{0}\}} = -1$, such that we can obtain all the matrix forms of the symmetry operators in the BdG system by using Eqs. 22-25 and Eq. 51. Combining the 3D lattice translation symmetries $\{E|100\}$, $\{E|010\}$, and $\{E|001\}$, we can obtain the superconducting pairing potentials by the Qsymm software package [49]:

$$\begin{aligned} B_{1u} : \mathcal{H}_{\Delta} &= \tilde{\Delta}_1 k_z \tau_x (\sigma_0 - \sigma_z) s_z \\ &+ \tilde{\Delta}_2 (k_x^2 - k_y^2) \left(-\sqrt{3} \tau_y \sigma_y s_z + \tau_x \sigma_y s_0 \right) \\ &- 2 \tilde{\Delta}_2 k_x k_y \left(\tau_y \sigma_y s_z + \sqrt{3} \tau_x \sigma_y s_0 \right), \end{aligned} \quad (57)$$

$$\begin{aligned} B_{2u} : \mathcal{H}_{\Delta} &= \Delta_1 k_z (\tau_y (\sigma_0 - \sigma_z) s_0) \\ &+ \Delta_2 (k_x^2 - k_y^2) \left(\tau_y \sigma_y s_z + \sqrt{3} \tau_x \sigma_y s_0 \right) \\ &- 2 \Delta_2 k_x k_y \left(\sqrt{3} \tau_y \sigma_y s_z - \tau_x \sigma_y s_0 \right). \end{aligned} \quad (58)$$

Since the B_{1u}/B_{2u} pairings share the same topological classification, we will discuss the B_{1u} pairing as an example. The $k.p$ model of the superconducting pairing potential can be extended to a tight-binding model, which is given by

TABLE V. Tight-binding parameters.

\tilde{M}_0	\tilde{M}_1	\tilde{M}_2	\tilde{A}	\tilde{B}	$\tilde{\mu}$	$\tilde{\Delta}_1$	$\tilde{\Delta}_2$
4	-1.5	-1	1	5	0.6	0.5	0.5

$$\begin{aligned}
\mathcal{H}_\Delta &= \tilde{\Delta}_1 \sin k_z \tau_x (\sigma_0 - \sigma_z) s_z \\
&+ \tilde{\Delta}_2 \left(\cos \frac{k_x}{2} \cos \frac{\sqrt{3}k_y}{2} - \cos k_x \right) \\
&\times \left(-\sqrt{3}\tau_y \sigma_y s_z + \tau_x \sigma_y s_0 \right) \\
&- \sqrt{3}\tilde{\Delta}_2 \sin \frac{k_x}{2} \sin \frac{\sqrt{3}k_y}{2} \left(\tau_y \sigma_y s_z + \sqrt{3}\tau_x \sigma_y s_0 \right).
\end{aligned} \tag{59}$$

The energies of the quasiparticle bands at Γ and A are given by

$$E(\bar{\Gamma}_9) = -E'(\bar{\Gamma}_{11}) = \left(\tilde{M}_0 + 2\tilde{M}_1 + 6\tilde{M}_2 \right) - \tilde{\mu}, \tag{60}$$

$$E(\bar{\Gamma}_{10}) = -E'(\bar{\Gamma}_7) = -\left(\tilde{M}_0 + 2\tilde{M}_1 + 6\tilde{M}_2 \right) - \tilde{\mu}, \tag{61}$$

$$E(\bar{A}_9) = -E'(\bar{A}_{11}) = \left(\tilde{M}_0 - 2\tilde{M}_1 + 6\tilde{M}_2 \right) - \tilde{\mu}, \tag{62}$$

$$E(\bar{A}_{10}) = -E'(\bar{A}_7) = -\left(\tilde{M}_0 - 2\tilde{M}_1 + 6\tilde{M}_2 \right) - \tilde{\mu}, \tag{63}$$

where $E(u_{\mathbf{k}}^\alpha)$ are the energies of the bands inherited from the normal states with coreps $u_{\mathbf{k}}^\alpha$, and $E'(u_{\mathbf{k}}^\alpha)$ are the energies of the corresponding BdG shadow bands related by the particle-hole symmetry in B_{1u} pairing channel. Given compatibility relations in Eq. 1, if the symmetry-enforced BdG Dirac crossings occur along DT, the energies of the Bloch states should satisfy $E(\bar{\Gamma}_9) \cdot E(\bar{A}_9) < 0$, i.e.,

$$|\tilde{M}_0 + 6\tilde{M}_2 - \tilde{\mu}| < 2|\tilde{M}_1|. \tag{64}$$

As a result, we can choose the parameters in Table IV to obtain a nodal Dirac superconducting state. The coreps of the Bloch states with $E < 0$ (ς_Γ) and $E > 0$ ($\bar{\varsigma}_\Gamma$) at Γ are given by

$$\varsigma_\Gamma = \bar{\Gamma}_9 \oplus \bar{\Gamma}_7, \tag{65}$$

$$\bar{\varsigma}_\Gamma = \bar{\Gamma}_{10} \oplus \bar{\Gamma}_{11}. \tag{66}$$

Similarly, the coreps of the Bloch states at A are given by

$$\varsigma_A = \bar{A}_{10} \oplus \bar{A}_{11}, \tag{67}$$

$$\bar{\varsigma}_A = \bar{A}_9 \oplus \bar{A}_7. \tag{68}$$

We assume that the value of the chemical potential $\tilde{\mu}$ is chosen to satisfy the half-filling normal states at each high-symmetry point, so the BdG symmetry data vector

can be determined by the small coreps with $E < 0$. We have neglected the symmetry data of the planes with $k_0 \pm \delta k_z$, since all the refined symmetry indicators vanish (see Supplementary Note 7 for details). The symmetry data vectors of the normal states have been given in Eqs. 42 and 43, thus those of the corresponding BdG shadow states are given by

$$\mathbf{B}'(0) = (1, 0, 0, 0, 0, 0, 0, 0, 1, 0, 1), \tag{69}$$

$$\mathbf{B}'(\pi) = (0, 0, 0, 0, 1, 0, 0, 0, 1, 0, 1), \tag{70}$$

Consequently, the BdG symmetry data vectors $\mathbf{B}^{\text{BdG}} = \mathbf{B} + \mathbf{B}'$ are respectively given by

$$\mathbf{B}^{\text{BdG}}(0) = (1, 0, 1, 0, 0, 0, 1, 0, 1, 0, 2), \tag{71}$$

$$\mathbf{B}^{\text{BdG}}(\pi) = (0, 0, 0, 1, 1, 0, 1, 0, 1, 0, 2). \tag{72}$$

Only one symmetry-enforced BdG Dirac point can occur in this four-band Hamiltonian according to the compatibility relations, as discussed in Sec. III. We can see this symmetry-enforced BdG Dirac point of the bulk spectrum in Fig. 4(a). Since the small coreps at DT is exchanged when we move k_z across the symmetry-enforced BdG Dirac points, the topological properties of the TRIM 2D planes with $k_z = 0$ and π will be changed.

Following the formula in Eq. 10, we can obtain the value of the conventional SI $z_6 = 0$ for both the planes with $k_z = 0, \pi$, such that there is no topological surface state, as shown in Fig. 4(b). However, as discussed in Ref. [37], the conventional SIs are not enough to distinguish all topologically nontrivial superconducting states. Following Supplementary Note 4, we can obtain

$$\chi_g(\{6_{001}^+|\mathbf{0}\})^* = \begin{pmatrix} e^{i5\pi/6} & & & \\ & e^{-i5\pi/6} & & \\ & & -i & \\ & & & i \end{pmatrix}, \tag{73}$$

$$\chi_g(\{\bar{1}|\mathbf{0}\})^* = \begin{pmatrix} -1 & & & \\ & -1 & & \\ & & 1 & \\ & & & 1 \end{pmatrix}, \tag{74}$$

$$\chi_g(\{6_{001}^+|\mathbf{0}\} \times \{\bar{1}|\mathbf{0}\})^* = \begin{pmatrix} e^{-i\pi/6} & & & \\ & e^{i\pi/6} & & \\ & & -i & \\ & & & i \end{pmatrix}, \tag{75}$$

such that the symmetry data vector of vacuum Hamiltonian is given by

$$\mathbf{B}^{\text{vac}} = (1, 0, 0, 0, 1, 0, 1, 0, 1, 1, 1). \tag{76}$$

The refined symmetry data vectors are

$$\mathbf{B}^{\text{BdG}}(0) - \mathbf{B}^{\text{vac}} = (0, 0, 1, 0, -1, 0, 0, 0, 0, -1, 1), \tag{77}$$

$$\mathbf{B}^{\text{BdG}}(\pi) - \mathbf{B}^{\text{vac}} = (-1, 0, 0, 1, 0, 0, 0, 0, 0, -1, 1). \tag{78}$$

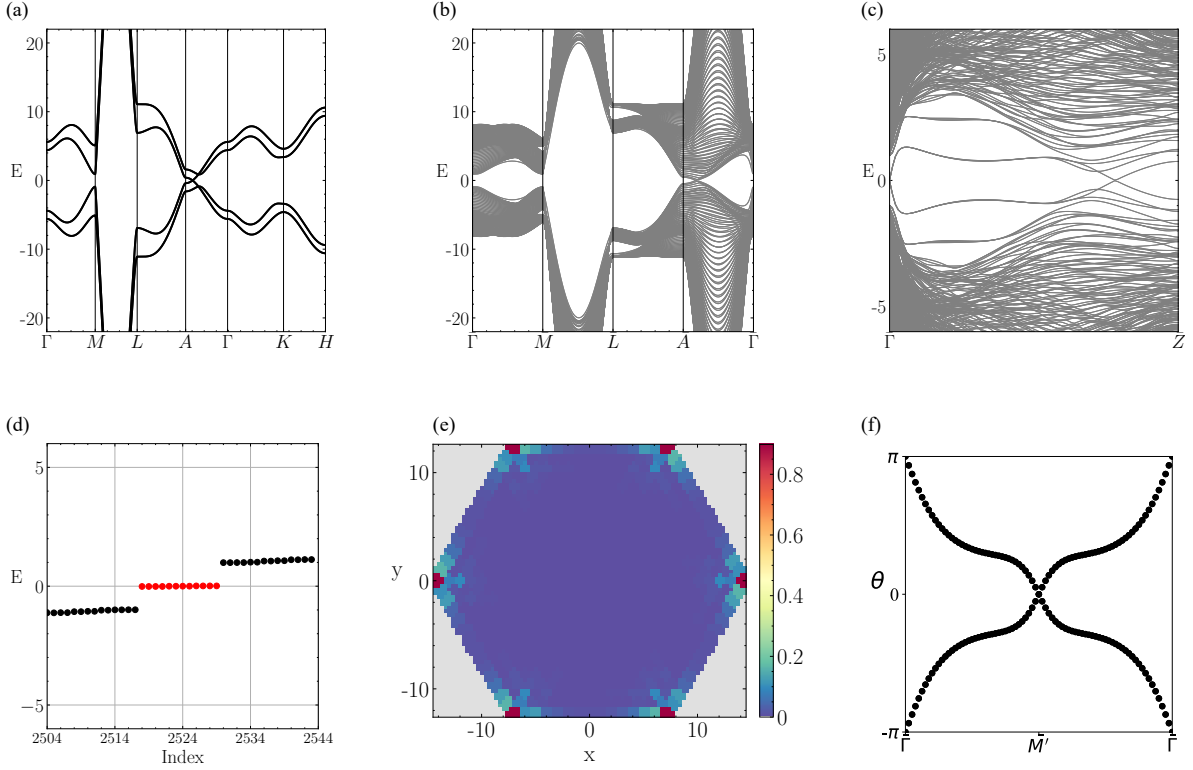


FIG. 5. (a) Bulk spectrum of the BdG Hamiltonian Eq. 48 with the normal state in Eq. 27 and B_{1u} superconducting pairing in Eq. 59. (b) Surface spectrum of of the tight-binding model in ribbon geometry when we terminate the 3D lattice in the a_2 direction. (c) Rod spectrum of the tight-binding model when we terminate the 3D lattice in the a_1 and a_2 directions. (d) Energy of the states at $k_z = 0$ of the tight-binding model in rod geometry. The red dots are the helical Majorana corner states composing the HOTDSC states. (e) Wave-function distribution of the mid-gap states (red dots in (d)) at $k_z = 0$. (f) a_2 -directed Wilson loops at $k_z = 0$ plotted as functions of kb_1 . All the figures are computed by the PythTb [50] and Kwant [51] software packages.

We can obtain $z_4 = 2$ for the 2D plane with $k_z = 0$, which means that it is not topologically trivial. But the 2D plane with $k_z = \pi$ is trivial since $z_4 = 0$. Using the formulas in Supplementary Notes 2, with $a_a = a'_a = 2$ the filling anomaly in Eq. 15 is $\eta^{\text{BdG}} = 6 \pmod{12}$ corresponding to the six helical MZMs at the six corners, as shown in Figs. 5(d) and 5(e). This result reveals that the 2D plane with $k_z = 0$ is an HOTDSC state.

When we calculate the a_2 -directed Wilson loop of the quasi-particle bands with $E < 0$, we find that it winds, as shown in Fig. 5(f). Although the Wilson loop is the same as the TCI with the mirror Chern number $C_{M_z} = 2$, there is no edge mode when we place the 2D plane on a ribbon geometry. Furthermore, this winding means that the quasi-particle bands are not Wannierizable, which indicates that the HOTDSC state does not characterize an obstructed atomic limit state as we analyzed in the normal state. Instead, this HOTDSC state is related to fragile topological states, whose Wilson loops can be trivialized by the introduction of trivial bands. The fragile topological superconducting states can be viewed as a nontrivial stacking of the original normal state with $C_{M_z} = 1$ and the corresponding BdG shadow state with

$C_{M_z} = -1$. The opposite values of the mirror Chern number for the normal state and the corresponding BdG shadow state indicate a gapped surface state in the BdG system. Specifically, for the corresponding BdG shadow bands, the symmetry data vector satisfies $\mathbf{B}' = \mathcal{E}\mathcal{B}\mathcal{R} \cdot \mathbf{p}'$ and the combination vector \mathbf{p}' is given by

$$\mathbf{p}' = \left(\frac{1}{2}, 0, -\frac{1}{2}, 0, -\frac{1}{2}, 0, 0, 0, 0, \frac{1}{2}, 0 \right) \pmod{2}, \quad (79)$$

By stacking \mathbf{p} for the normal state in Eq. 47 together, we can obtain the combination vector for the nodal Dirac superconducting state,

$$\begin{aligned} \mathbf{p}^{\text{BdG}} &= \mathbf{p} + \mathbf{p}' \\ &= (0, 0, -1, 0, 0, 0, 0, 0, 0, 1, 0) \pmod{4}, \end{aligned} \quad (80)$$

which also shows that this is a fragile topological superconducting state and unstable to the addition of $\Delta\mathbf{p} = (0, 0, 1, 0, 0, 0, 0, 0, 0, 0, 0) \pmod{2}$ corresponding to an additional EBR $(\bar{E}_{2g})_{1a} \uparrow G = \bar{\Gamma}_8 \oplus \bar{K}_8 \oplus \bar{M}_5$. This result indicates that a spinful d orbital at $1a$ Wyckoff position can trivialize the fragile topological superconducting state. Unlike the fragile states of 2D

insulators which need to break the mirror symmetry M_z in Ref. [9], the fragile superconducting states here need to preserve M_z to protect the TCI states in normal states and BdG shadow states. Thus the fragile topological superconducting states would stem from the nontrivial stacking of these two TCIs. Since the HOFAs in normal and BdG shadow states always connect to the projected surface states at $k_z = 0$, the HOTDSC states can be regarded as a crossing of the HOFAs, as shown in Fig. 5(c). As a result, for nodal superconductors respecting $P6/mmm1'$, this kind of HOTDSCs can only arise from HOFA DSM normal states with B_{1u}/B_{2u} pairing representations as discussed in Sec. III, which is protected by the symmetries $\{6_{001}^+|\mathbf{0}\}$, $\{\bar{1}|\mathbf{0}\}$, $\{m_{001}|\mathbf{0}\}$ and $\{1'|\mathbf{0}\}$ in the BdG system.

V. DISCUSSION

In this work, we utilize the theory of MTQC to systematically discuss the possible HOTDSC phases in DSMs respecting Type-II SSG $P6/mmm1'$. Our results advance the classification of Dirac points in Ref. [11] to nodal Dirac superconducting systems. We also reveal the relationship between HOFAs and HOTDSCs at TRIM planes.

The occurrence of Dirac points in DSMs can be determined by compatibility relations. These Dirac points can be regarded as critical points between obstructed atomic insulators and trivial phases. Thus the Dirac points can be classified by the relative topology. We found that the Dirac points can be inherited by the superconducting states, which would lead to the BdG Dirac points. We also found that not all the BdG Dirac points host nontrivial relative topology. Only the symmetry-enforced BdG Dirac points can be related to HOTDSC states.

For the superconducting states in DSMs respecting Type-II SSG $P6/mmm1'$, our calculation showed that all the refined SIs vanish along the high-symmetry line DT. Thus the BdG Dirac points in these systems do not exhibit HOMAs as those in Ref. [26]. Instead,

the HOTDSC states would occur at the TRIM planes. For the symmetry-enforced nodal Dirac superconducting states, the HOTDSC states can be viewed as a crossing of the HOFAs in normal states and BdG shadow states. We also utilized the relative topology to determine whether the HOTDSC states would occur in superconductors with and without symmetry-enforced BdG Dirac points respecting Type-II SSG $P6/mmm1'$. We found that for symmetry-enforced nodal Dirac superconducting states, the HOTDSC states can only arise from the HOFA DSMs with B_{1u}/B_{2u} pairing representations, which can be indicated by their relative topologies.

Different from that the HOFA states in DSMs are OAL states, the HOTDSC states in symmetry-enforced nodal Dirac superconductors are fragile topological superconducting states. The HOTDSC states can be viewed as a nontrivial stacking of two TCIs with opposite mirror Chern numbers. We deduce that the HOTDSC states in symmetry-enforced nodal Dirac superconducting states are the topological bulk-hinge correspondence for the symmetry-enforced BdG Dirac points.

Moreover, superconducting states without symmetry-enforced BdG Dirac points can also exhibit HOTDSC states. These HOTDSC states are not the topological consequence of symmetry-enforced BdG Dirac points. The change in the symmetry data vectors between the 2D planes with $k_z = 0$ and $k_z = \pi$ arise from the different subduced small cores at Γ . Although this difference may lead neither to symmetry-enforced Dirac points in normal states nor to symmetry-enforced BdG Dirac points in superconducting states, HOTDSC states can still exist, which can also be indicated by their relative topologies.

VI. ACKNOWLEDGMENTS

We would like to thank Zhongbo Yan and Cui-Qun Chen for helpful discussions. This work is supported by Guangdong Basic and Applied Basic Research Foundation (Grants No. 2023A1515110002).

-
- [1] T. Zhang, Y. Jiang, Z. Song, H. Huang, Y. He, Z. Fang, H. Weng, and C. Fang, Catalogue of topological electronic materials, *Nature* **566**, 475 (2019).
 - [2] Z. Song, Z. Wang, W. Shi, G. Li, C. Fang, and B. A. Bernevig, All Magic Angles in Twisted Bilayer Graphene are Topological, *Physical Review Letters* **123**, 036401 (2019).
 - [3] Z. Wang, Y. Sun, X.-Q. Chen, C. Franchini, G. Xu, H. Weng, X. Dai, and Z. Fang, Dirac semimetal and topological phase transitions in $\{A\}_3\text{Bi}$ ($A=\text{Na}, \text{K}, \text{Rb}$), *Physical Review B* **85**, 195320 (2012).
 - [4] J. Xiao and B. Yan, First-principles calculations for topological quantum materials, *Nature Reviews Physics* **3**, 283 (2021).
 - [5] Y. Xu, L. Elcoro, Z.-D. Song, B. J. Wieder, M. G. Vergniory, N. Regnault, Y. Chen, C. Felser, and B. A. Bernevig, High-throughput calculations of magnetic topological materials, *Nature* **586**, 702 (2020).
 - [6] J. Kruthoff, J. de Boer, J. van Wezel, C. L. Kane, and R.-J. Slager, Topological classification of crystalline insulators through band structure combinatorics, *Phys. Rev. X* **7**, 041069 (2017).
 - [7] A. Tamai, Q. Wu, I. Cucchi, F. Bruno, S. Riccò, T. Kim, M. Hoesch, C. Barreteau, E. Giannini, C. Besnard,

- A. Soluyanov, and F. Baumberger, Fermi Arcs and Their Topological Character in the Candidate Type-II Weyl Semimetal MoTe₂, *Physical Review X* **6**, 031021 (2016).
- [8] Y. Kim, B. J. Wieder, C. Kane, and A. M. Rappe, Dirac Line Nodes in Inversion-Symmetric Crystals, *Physical Review Letters* **115**, 036806 (2015).
- [9] B. J. Wieder, Z. Wang, J. Cano, X. Dai, L. M. Schoop, B. Bradlyn, and B. A. Bernevig, Strong and fragile topological Dirac semimetals with higher-order Fermi arcs, *Nature Communications* **11**, 627 (2020).
- [10] M. Lin and T. L. Hughes, Topological quadrupolar semimetals, *Physical Review B* **98**, 241103 (2018).
- [11] Y. Fang and J. Cano, Classification of Dirac points with higher-order Fermi arcs, *Physical Review B* **104**, 245101 (2021).
- [12] R.-J. Slager, A. Mesáros, V. Juričić, and J. Zaanen, The space group classification of topological band-insulators, *Nature Physics* **9**, 98 (2013).
- [13] Y. Fang and J. Cano, Filling anomaly for general two- and three-dimensional C₄ symmetric lattices, *Physical Review B* **103**, 165109 (2021).
- [14] J. Gao, Y. Qian, H. Jia, Z. Guo, Z. Fang, M. Liu, H. Weng, and Z. Wang, Unconventional materials: the mismatch between electronic charge centers and atomic positions, *Science Bulletin* **67**, 598 (2022).
- [15] D.-S. Ma, K. Yu, X.-P. Li, X. Zhou, and R. Wang, Obstructed atomic insulators with robust corner modes, *Physical Review B* **108**, L100101 (2023).
- [16] F. Schindler, A. M. Cook, M. G. Vergniory, Z. Wang, S. S. P. Parkin, B. A. Bernevig, and T. Neupert, Higher-order topological insulators, *Science Advances* **4**, eaat0346 (2018).
- [17] D. Călugăru, V. Juričić, and B. Roy, Higher-order topological phases: A general principle of construction, *Physical Review B* **99**, 041301 (2019).
- [18] M. G. Vergniory, L. Elcoro, C. Felser, N. Regnault, B. A. Bernevig, and Z. Wang, A complete catalogue of high-quality topological materials, *Nature* **566**, 480 (2019).
- [19] J. Cano and B. Bradlyn, Band Representations and Topological Quantum Chemistry, *Annual Review of Condensed Matter Physics* **12**, 225 (2021).
- [20] F. Tang, H. C. Po, A. Vishwanath, and X. Wan, Comprehensive search for topological materials using symmetry indicators, *Nature* **566**, 486 (2019).
- [21] F. Tang, H. C. Po, A. Vishwanath, and X. Wan, Efficient topological materials discovery using symmetry indicators, *Nature Physics* **15**, 470 (2019).
- [22] B. Bradlyn, L. Elcoro, J. Cano, M. G. Vergniory, Z. Wang, C. Felser, M. I. Aroyo, and B. A. Bernevig, Topological quantum chemistry, *Nature* **547**, 298 (2017).
- [23] F. Tang, H. C. Po, A. Vishwanath, and X. Wan, Towards ideal topological materials: Comprehensive database searches using symmetry indicators, *Nature* **566**, 486 (2019).
- [24] R.-X. Zhang, Y.-T. Hsu, and S. Das Sarma, Higher-order topological Dirac superconductors, *Physical Review B* **102**, 094503 (2020).
- [25] J. Ahn and B.-J. Yang, Higher-order topological superconductivity of spin-polarized fermions, *Physical Review Research* **2**, 012060 (2020).
- [26] Z. Wu and Y. Wang, Nodal higher-order topological superconductivity from a C_4 -symmetric Dirac semimetal, *Physical Review B* **106**, 214510 (2022).
- [27] D. Agterberg, P. Brydon, and C. Timm, Bogoliubov Fermi Surfaces in Superconductors with Broken Time-Reversal Symmetry, *Physical Review Letters* **118**, 127001 (2017).
- [28] F. Tang, S. Ono, X. Wan, and H. Watanabe, High-Throughput Investigations of Topological and Nodal Superconductors, *Physical Review Letters* **129**, 027001 (2022).
- [29] Y.-T. Hsu, W. S. Cole, R.-X. Zhang, and J. D. Sau, Inversion-Protected Higher-Order Topological Superconductivity in Monolayer WTe_2 , *Physical Review Letters* **125**, 097001 (2020).
- [30] H. C. Po, H. Watanabe, and A. Vishwanath, Fragile Topology and Wannier Obstructions, *Physical Review Letters* **121**, 126402 (2018).
- [31] Z. Song, T. Zhang, Z. Fang, and C. Fang, Quantitative mappings between symmetry and topology in solids, *Nature Communications* **9**, 3530 (2018).
- [32] E. Khalaf, H. C. Po, A. Vishwanath, and H. Watanabe, Symmetry Indicators and Anomalous Surface States of Topological Crystalline Insulators, *Physical Review X* **8**, 031070 (2018).
- [33] H. C. Po, A. Vishwanath, and H. Watanabe, Symmetry-based indicators of band topology in the 230 space groups, *Nature Communications* **8**, 1 (2017).
- [34] A. Skurativska, T. Neupert, and M. H. Fischer, Atomic limit and inversion-symmetry indicators for topological superconductors, *Physical Review Research* **2**, 013064 (2020).
- [35] S. Ono, Y. Yanase, and H. Watanabe, Symmetry indicators for topological superconductors, *Physical Review Research* **1**, 013012 (2019).
- [36] S. Ono, H. C. Po, and K. Shiozaki, Z₂-enriched symmetry indicators for topological superconductors in the 1651 magnetic space groups, *Physical Review Research* **3**, 023086 (2021).
- [37] S. Ono, H. C. Po, and H. Watanabe, Refined symmetry indicators for topological superconductors in all space groups, *Science Advances* **6**, eaaz8367 (2020).
- [38] Y.-B. Yang, J.-H. Wang, K. Li, and Y. Xu, Higher-order topological phases in crystalline and non-crystalline systems: a review, *Journal of Physics: Condensed Matter* **36**, 283002 (2024).
- [39] S. Manna, S. Nandy, and B. Roy, Higher-order topological phases on fractal lattices, *Phys. Rev. B* **105**, L201301 (2022).
- [40] S. Manna and B. Roy, Inner skin effects on non-Hermitian topological fractals, *Communications Physics* **6**, 10 (2023).
- [41] S. Manna, S. K. Das, and B. Roy, Noncrystalline topological superconductors, *Phys. Rev. B* **109**, 174512 (2024).
- [42] M. I. Aroyo, A. Kirov, C. Capillas, J. M. Perez-Mato, and H. Wondratschek, Bilbao Crystallographic Server. II. Representations of crystallographic point groups and space groups, *Acta Crystallographica Section A: Foundations of Crystallography* **62**, 115 (2006).
- [43] M. I. Aroyo, J. M. Perez-Mato, C. Capillas, E. Kroumova, S. Ivantchev, G. Madariaga, A. Kirov, and H. Wondratschek, Bilbao Crystallographic Server: I. Databases and crystallographic computing programs, *Zeitschrift für Kristallographie - Crystalline Materials* **221**, 15 (2006).

- [44] A. Lau, R. Ray, D. Varjas, and A. Akhmerov, The influence of lattice termination on the edge states of the quantum spin Hall insulator monolayer $\text{1T}'\text{-WTe}_2$, *Physical Review Materials* **3**, 054206 (2019).
- [45] S. K. Das, S. Manna, and B. Roy, Topologically distinct atomic insulators, *Phys. Rev. B* **108**, L041301 (2023).
- [46] B. Bradlyn, Z. Wang, J. Cano, and B. A. Bernevig, Disconnected elementary band representations, fragile topology, and Wilson loops as topological indices: An example on the triangular lattice, *Physical Review B* **99**, 045140 (2019).
- [47] Z.-D. Song, L. Elcoro, Y.-F. Xu, N. Regnault, and B. A. Bernevig, Fragile Phases as Affine Monoids: Classification and Material Examples, *Physical Review X* **10**, 031001 (2020).
- [48] A. Bouhon, A. M. Black-Schaffer, and R.-J. Slager, Wilson loop approach to fragile topology of split elementary band representations and topological crystalline insulators with time-reversal symmetry, *Phys. Rev. B* **100**, 195135 (2019).
- [49] D. Varjas, T. O. Rosdahl, and A. R. Akhmerov, Qsymm: Algorithmic symmetry finding and symmetric Hamiltonian generation, *New Journal of Physics* **20**, 093026 (2018).
- [50] S. Coh and D. Vanderbilt, *Python Tight Binding (PythTB)* (2022).
- [51] C. W. Groth, M. Wimmer, A. R. Akhmerov, and X. Waintal, Kwant: a software package for quantum transport, *New Journal of Physics* **16**, 063065 (2014).